

# Proper Orthogonal Descriptors for Multi-element Chemical Systems

Ngoc-Cuong Nguyen<sup>a</sup>

<sup>a</sup>*Center for Computational Engineering, Department of Aeronautics and Astronautics,  
Massachusetts Institute of Technology, 77 Massachusetts  
Avenue, Cambridge, MA, 02139, USA*

---

## Abstract

We introduce the proper orthogonal descriptors for efficient and accurate interatomic potentials of multi-element chemical systems. The potential energy surface of a multi-element system is represented as a many-body expansion of parametrized potentials which are functions of atom positions, atom types, and parameters. The Karhunen-Loève expansion is employed to decompose the parametrized potentials into a set of orthogonal basis functions. The orthogonal basis functions are used to construct proper orthogonal descriptors based on the elements of atoms, thus leading to multi-element descriptors. For a system of  $N_e$  elements, the number of multi-element proper orthogonal descriptors increases as  $O(N_e^3)$ , while the computational cost is independent of  $N_e$ . We compose the multi-element proper orthogonal descriptors to develop two different interatomic potentials. The first potential expresses the energy of each atom as a linear combination of proper orthogonal descriptors, while the second potential expresses the energy as a linear and quadratic combination of the descriptors. The second potential is shown to provide a significant increase in accuracy relative to the first potential, while having the same computational complexity as the first potential. The proposed potentials are demonstrated for indium phosphide and titanium dioxide in comparison with the spectral neighbor analysis potential (SNAP) and atomic cluster expansion (ACE) potentials.

**Keywords:** interatomic potentials, machine learning potentials, Karhunen-Loève expansion, proper orthogonal descriptors, atomic cluster expansion, spectral neighbor analysis potential

---

## 1. Introduction

Multi-element systems such as alloys, compounds, and composite materials are used in numerous applications and products. The properties of these classes of materials vary with both chemical structures and component compositions. *Ab initio* methods for self-consistent calculation of the electronic structures provide the most accurate modeling technique to understanding physical and chemical properties of multi-element systems. As *ab initio* methods can be extremely expensive due to their high computational complexity, they are restricted to solving small-scale systems with thousands of atoms at most. Interatomic potentials represent the potential energy surface of a system as a function of atomic positions and types, leaving out the detailed electronic structures. As most interatomic potentials have a computational complexity that scales linearly with the number of atoms, they enable molecular dynamics simulations of large-scale systems with millions or even billions of atoms.

An interatomic potential is essentially a mathematical model that takes the full quantum many-body problem and casts it into computationally tractable expressions for the total energy as the sum of individual atom contributions. However, this simplification can be done in many different ways, giving rise to the numerous different types of interatomic potentials in the literature. The simplest and most efficient potentials are two-body potentials which express the energies and forces solely in terms of pairwise interactions between nearby atoms. Over the years, sophisticated empirical potentials have been developed to treat a wide variety of systems with different degrees of complexity. More often than not, existing empirical potentials are recalibrated by reparameterizing the existing set of parameters or extending the energy formula by adding terms and then parameterizing the entire potential anew. This results in many different forms and sets of parameters for widely-used empirical potentials such as EAM [1], Stillinger-Weber [2], Tersoff [3], EDIP [4], REBO [5], ReaxFF [6].

In recent years, a significant trend has emerged in the form of machine learning (ML) interatomic potentials, where the potential energy surface is described as a composition of local environment descriptors [7, 8, 9]. In order to obtain an accurate and efficient ML potential, the descriptors must meet several requirements. First and foremost, the descriptors must be invariant with respect to permutation, rotation, translation, and reflection of atoms in the system. Second, the descriptors need to be differentiable with

respect to the atomic positions to enable the calculation of analytic gradients for the forces. Third, the descriptors must provide a detailed structural description of the local atomic environment to produce accurate and transferable potentials. Lastly, since the transformation from atom coordinates onto the descriptors has to be carried out for every atom, the computation of the descriptors has to be fast to produce efficient potentials. Examples of ML potentials include the neural network potential (NNP) [10, 11, 12], the Gaussian approximation potential (GAP) [13, 14, 15], the spectral neighbor analysis potential (SNAP) [16, 17], moment tensor potentials (MTP) [18, 19], and the atomic cluster expansion (ACE) [20, 21, 9]. A recent work [22] assesses performance of SNAP, GAP, NNP, MTP potentials on a diverse dataset of bcc and fcc metals, as well as diamond group IV semiconductors.

In a recent work [23], we introduce a new method to represent atomic neighbourhood environments with the so-called proper orthogonal descriptors (PODs) inspired by the reduced basis method [24, 25, 26, 27, 28] for parametrized partial differential equations. The POD potential is expressed as a linear combination of the proper orthogonal descriptors and fitted against density functional theory (DFT) data by using least-squares regression. The POD potential is demonstrated on single-element systems of Li, Mo, Cu, Ni, Si, Ge, Ta elements and found to provide more accurate predictions than both SNAP and ACE potentials on majority of cases.

In this paper, we extend our previous work [23] to develop proper orthogonal descriptors for multi-element chemical systems. The potential energy surface of a multi-element system is represented as a many-body expansion of parametrized potentials which are functions of atom positions, atom types, and parameters. The orthogonal basis functions are formed by using Karhunen-Loève (KL) expansion of the parametrized potentials and transformed into proper orthogonal descriptors according to the chemical elements of atoms, thus leading to multi-element descriptors. For a system of  $N_e$  elements, the number of multi-element proper orthogonal descriptors increases as  $O(N_e^3)$ , while the computational cost is independent of  $N_e$ . Furthermore, we introduce two different POD potentials for multi-element systems by composing the descriptors in two different ways. The first POD potential is expressed as a linear combination of the descriptors. To develop the second POD potential, we compose the original descriptors to construct new descriptors that can capture higher-body interactions and provide more accurate predictions. While the second POD potential has an order of magnitude more descriptors than the first POD potential, it has exactly the same com-

putational complexity as the first one. The two POD potentials are demonstrated for indium phosphide and titanium dioxide in comparison with the spectral neighbor analysis potential (SNAP) and atomic cluster expansion (ACE) potentials. The second POD potential is found to be considerably more accurate than the first POD potential, SNAP and ACE potentials.

The paper is organized as follows. We introduce multi-element proper orthogonal descriptors in Section 2 and develop the two POD potentials in Section 3. In Section 4, we describe an optimization procedure to fit POD potentials. In Section 5, we present numerical results to assess the performance of not only the POD potentials but also the ACE and SNAP potentials. Finally, in Section 6, we make a number of concluding remarks on the results as well as future work.

## 2. Multi-Element Proper Orthogonal Descriptors

### 2.1. Parametrized potential energy surface

We consider a multi-element system of  $N$  atoms with  $N_e$  unique elements. We denote by  $\mathbf{r}_n$  and  $Z_n$  position vector and type of an atom  $n$  in the system, respectively. Note that we have  $Z_n \in \{1, \dots, N_e\}$ ,  $\mathbf{R} = (\mathbf{r}_1, \mathbf{r}_2, \dots, \mathbf{r}_N) \in \mathbb{R}^{3N}$ , and  $\mathbf{Z} = (Z_1, Z_2, \dots, Z_N) \in \mathbb{N}^N$ . The potential energy surface (PES) of the system can be expressed as a many-body expansion of the form

$$\begin{aligned} E(\mathbf{R}, \mathbf{Z}, \boldsymbol{\eta}, \boldsymbol{\mu}) = & \sum_i V^{(1)}(\mathbf{r}_i, Z_i, \boldsymbol{\mu}^{(1)}) + \frac{1}{2} \sum_{i,j} V^{(2)}(\mathbf{r}_i, \mathbf{r}_j, Z_i, Z_j, \boldsymbol{\eta}, \boldsymbol{\mu}^{(2)}) \\ & + \frac{1}{6} \sum_{i,j,k} V^{(3)}(\mathbf{r}_i, \mathbf{r}_j, \mathbf{r}_k, Z_i, Z_j, Z_k, \boldsymbol{\eta}, \boldsymbol{\mu}^{(3)}) + \dots \end{aligned} \quad (1)$$

where  $V^{(1)}$  is the one-body potential often used for representing external field or energy of isolated elements, and the higher-body potentials  $V^{(2)}, V^{(3)}, \dots$  are symmetric, uniquely defined, and zero if two or more indices take identical values. The superscript on each potential denotes its body order. Each  $q$ -body potential  $V^{(q)}$  depends on  $\boldsymbol{\mu}^{(q)}$  which are sets of parameters to fit the PES. Note that  $\boldsymbol{\mu}$  is a collection of all potential parameters  $\boldsymbol{\mu}^{(1)}, \boldsymbol{\mu}^{(2)}, \boldsymbol{\mu}^{(3)}$ , etc, and that  $\boldsymbol{\eta}$  is a set of hyperparameters such as inner cut-off radius  $r_{\min}$  and outer cut-off radius  $r_{\max}$ .

In the absence of external fields, the PES should not depend on the absolute position of atoms, but only on the relative positions. This means

that the PES can be rewritten as a function of interatomic distances and angles between the bonds as

$$\begin{aligned}
E(\mathbf{R}, \mathbf{Z}, \boldsymbol{\eta}, \boldsymbol{\mu}) = & \sum_i V^{(1)}(Z_i, \boldsymbol{\mu}^{(1)}) + \frac{1}{2} \sum_{i,j} V^{(2)}(r_{ij}, Z_i, Z_j, \boldsymbol{\eta}, \boldsymbol{\mu}^{(2)}) \\
& + \frac{1}{6} \sum_{i,j,k} V^{(3)}(r_{ij}, r_{ik}, \theta_{ijk}, Z_i, Z_j, Z_k, \boldsymbol{\eta}, \boldsymbol{\mu}^{(3)}) + \dots
\end{aligned} \tag{2}$$

where each potential is a function of interatomic distances  $r_{ij} = |\mathbf{r}_i - \mathbf{r}_j|$ , bond angles  $\theta_{ijk}$ , potential parameters, and the hyperparameters.

A wide variety of interatomic potentials such as Lennard-Jones potential, Morse potential, Stillinger-Weber potential, angle potentials, and dihedral potentials have the form (2). For these empirical potentials, however, both  $\boldsymbol{\eta}$  and  $\boldsymbol{\mu}$  are fixed to specific values. In other interatomic potentials such as EAM and Tersoff potentials, the many-body interactions are embedded into the terms of a pair potential in which the nature of the interaction is modified by the local environment of the atom via the bond order parameter, coordination number, or electron density.

Interatomic potentials rely on parameters to learn relationship between atomic environments and interactions. Since interatomic potentials are approximations by nature, their parameters need to be set to some reference values or fitted against experimental and/or numerical data by necessity. In simple potentials such as the Lennard-Jones and Morse potential, the parameters can be set to match the equilibrium bond length and bond strength of a dimer molecule or the surface energy of a solid. Many-body potentials often contain many parameters with limited interpretability and need to be optimized by fitting their parameters against a larger set of data. Typically, potential fitting finds optimal parameters,  $\boldsymbol{\mu}^*$ , to minimize a certain loss function of the predicted quantities and data. Since the fitted potential depends on the data set used to fit it, different data sets will yield different optimal parameters and thus different fitted potentials. When fitting the same functional form on  $Q$  different data sets, we would obtain  $Q$  different optimized potentials,  $E(\mathbf{R}, \mathbf{Z}, \boldsymbol{\eta}, \boldsymbol{\mu}_q^*)$ ,  $1 \leq q \leq Q$ . These optimized potentials are typically intended to predict properties that are similar to those they are fitted to. Inaccurate predictions may occur when they are used to predict out-of-fitting properties. Consequently, there exist many different sets of optimized parameters for widely-used empirical potentials such as EAM [1], Stillinger-Weber [2], Tersoff [3], EDIP [4], REBO [5], ReaxFF [6].

Instead of finding optimal parameters for the PES (2), inspired by the reduced basis method [24, 25, 26, 27, 28] for parametrized partial differential equations, we propose to view the parametrized PES as a parametric manifold of potential energies

$$\mathcal{M} = \{E(\mathbf{R}, \mathbf{Z}, \boldsymbol{\eta}, \boldsymbol{\mu}) \mid \boldsymbol{\mu} \in \Omega^\mu\} \quad (3)$$

where  $\Omega^\mu$  is a parameter domain in which  $\boldsymbol{\mu}$  resides. The parametric manifold  $\mathcal{M}$  contains potential energy surfaces for all values of  $\boldsymbol{\mu} \in \Omega^\mu$ . Therefore, the parametric manifold yields a much richer and more transferable atomic representation than any particular individual PES  $E(\mathbf{R}, \mathbf{Z}, \boldsymbol{\eta}, \boldsymbol{\mu}^*)$ .

In this section, we propose specific forms of the parametrized potentials for one-body, two-body, and three-body interactions. We then apply the KL expansion to snapshots of the parametrized potentials to obtain sets of orthogonal basis functions. These basis functions are aggregated into PODs according to the chemical elements of atoms, thus leading to multi-element descriptors. Finally, we discuss the computational complexity of the PODs and their derivatives with respect to atom positions.

### 2.2. One-body descriptors

The descriptors for the one-body interaction are used to capture energy of isolated elements and defined as follows

$$D_{ip}^{(1)} = \begin{cases} 1, & \text{if } Z_i = p \\ 0, & \text{if } Z_i \neq p \end{cases} \quad (4)$$

for  $1 \leq i \leq N, 1 \leq p \leq N_e$ . The number of one-body descriptors per atom is equal to the number of elements. The one-body descriptors are independent of atom positions, but dependent on atom types.

### 2.3. Two-body proper orthogonal descriptors

We adopt the usual assumption that the direct interaction between two atoms vanishes smoothly when their distance is greater than the outer cutoff distance  $r_{\max}$ . Furthermore, we assume that two atoms can not get closer than the inner cutoff distance  $r_{\min}$  due to the Pauli repulsion principle. Let  $r \in (r_{\min}, r_{\max})$ , we introduce the following parametrized radial functions

$$\phi(r, r_{\min}, r_{\max}, \alpha, \beta) = \frac{\sin(\alpha\pi x)}{r - r_{\min}}, \quad \varphi(r, \gamma) = \frac{1}{r^\gamma}, \quad (5)$$

where the scaled distance function  $x$  is defined below to enrich the two-body manifold

$$x(r, r_{\min}, r_{\max}, \beta) = \frac{e^{-\beta(r-r_{\min})/(r_{\max}-r_{\min})} - 1}{e^{-\beta} - 1}. \quad (6)$$

We introduce the following function as a convex combination of the two functions in (5)

$$\psi(r, r_{\min}, r_{\max}, \alpha, \beta, \gamma, \kappa) = \kappa \phi(r, r_{\min}, r_{\max}, \alpha, \beta) + (1 - \kappa) \varphi(r, \gamma). \quad (7)$$

We see that  $\psi$  is a function of distance  $r$ , cut-off distances  $r_{\min}$  and  $r_{\max}$ , and parameters  $\alpha, \beta, \gamma, \kappa$ . Together these parameters allow the function  $\psi$  to characterize a diverse spectrum of two-body interactions within the cut-off interval  $(r_{\min}, r_{\max})$ .

Next, we introduce the following parametrized potential

$$W^{(2)}(r_{ij}, \boldsymbol{\eta}, \boldsymbol{\mu}^{(2)}) = f_c(r_{ij}, \boldsymbol{\eta}) \psi(r_{ij}, \boldsymbol{\eta}, \boldsymbol{\mu}^{(2)}) \quad (8)$$

where  $\eta_1 = r_{\min}, \eta_2 = r_{\max}, \mu_1^{(2)} = \alpha, \mu_2^{(2)} = \beta, \mu_3^{(2)} = \gamma$ , and  $\mu_4^{(2)} = \kappa$ . Here the cut-off function  $f_c(r_{ij}, \boldsymbol{\eta})$  proposed in [23] is used to ensure the smooth vanishing of the potential and its derivative for  $r_{ij} \geq r_{\max}$ :

$$f_c(r_{ij}, r_{\min}, r_{\max}) = \exp \left( 1 - \frac{1}{\sqrt{\left(1 - \frac{(r-r_{\min})^3}{(r_{\max}-r_{\min})^3}\right)^2 + 10^{-6}}} \right). \quad (9)$$

Based on the parametrized potential (8), we form a set of snapshots as follows. We assume that we are given  $N_s$  parameter tuples  $\boldsymbol{\mu}_\ell^{(2)}, 1 \leq \ell \leq N_s$ . We introduce the following set of snapshots on  $(r_{\min}, r_{\max})$ :

$$\xi_\ell(r_{ij}, \boldsymbol{\eta}) = W^{(2)}(r_{ij}, \boldsymbol{\eta}, \boldsymbol{\mu}_\ell^{(2)}), \quad \ell = 1, \dots, N_s. \quad (10)$$

To ensure adequate sampling of the PES for different parameters, we choose  $N_s$  parameter points  $\boldsymbol{\mu}_\ell^{(2)} = (\alpha_\ell, \beta_\ell, \gamma_\ell, \kappa_\ell), 1 \leq \ell \leq N_s$  as follows. The parameters  $\alpha \in [1, N_\alpha]$  and  $\gamma \in [1, N_\gamma]$  are integers, where  $N_\alpha$  and  $N_\gamma$  are the highest degrees for  $\alpha$  and  $\gamma$ , respectively. We next choose  $N_\beta$  different values of  $\beta$  in the interval  $[\beta_{\min}, \beta_{\max}]$ , where  $\beta_{\min} = 0$  and  $\beta_{\max} = 4$ . The parameter  $\kappa$  can be set either 0 or 1. Hence, the total number of parameter points is  $N_s = N_\alpha N_\beta + N_\gamma$ . Although  $N_\alpha, N_\beta, N_\gamma$  can be chosen conservatively

large, we find that  $N_\alpha = 6$ ,  $N_\beta = 3$ ,  $N_\gamma = 8$  are adequate for most problems. At this point,  $r_{\min}$  and  $r_{\max}$  are assumed to be given. As discussed later they are found by solving an outer optimization problem.

We employ the Karhunen-Loève (KL) expansion [29] to generate an orthogonal basis set which is known to be optimal for representation of the snapshot family  $\{\xi_\ell\}_{\ell=1}^{N_s}$ . The two-body orthogonal basis functions are computed as follows

$$U_m^{(2)}(r_{ij}, \boldsymbol{\eta}) = \sum_{\ell=1}^{N_s} A_{\ell m}(\boldsymbol{\eta}) \xi_\ell(r_{ij}, \boldsymbol{\eta}), \quad m = 1, \dots, N_{2b}, \quad (11)$$

where the matrix  $\mathbf{A} \in \mathbb{R}^{N_s \times N_s}$  consists of eigenvectors of the eigenvalue problem

$$\mathbf{C}\mathbf{a} = \lambda\mathbf{a}, \quad (12)$$

where the entries of  $\mathbf{C} \in \mathbb{R}^{N_s \times N_s}$  are given by

$$C_{ij} = \frac{1}{N_s} \int_{r_{\min}}^{r_{\max}} \xi_i(x, \boldsymbol{\eta}) \xi_j(x, \boldsymbol{\eta}) dx, \quad 1 \leq i, j \leq N_s.$$

Note that the eigenvalues  $\lambda_\ell$ ,  $1 \leq \ell \leq N_s$ , are ordered such that  $\lambda_1 \geq \lambda_2 \geq \dots \geq \lambda_{N_s}$ , and that the matrix  $\mathbf{A}$  is pre-computed and stored for any given  $\boldsymbol{\eta}$ . Owing to the rapid convergence of the KL expansion, only a small number of orthogonal basis functions is needed to obtain accurate approximation. Typically, we choose  $N_{2b}$  less than or equal to 10.

Finally, the two-body proper orthogonal descriptors at each atom  $i$  are computed by summing the orthogonal basis functions over the neighbors of atom  $i$  and numerating on the atom types as follows

$$D_{iml(p,q)}^{(2)}(\boldsymbol{\eta}) = \begin{cases} \sum_{\{j|Z_j=q\}} U_m^{(2)}(r_{ij}, \boldsymbol{\eta}), & \text{if } Z_i = p \\ 0, & \text{if } Z_i \neq p \end{cases} \quad (13)$$

for  $1 \leq i \leq N$ ,  $1 \leq m \leq N_{2b}$ ,  $1 \leq q, p \leq N_e$ . Here  $l(p, q)$  is a symmetric index mapping such that

$$l(p, q) = \begin{cases} q + (p-1)N_e - p(p-1)/2, & \text{if } q \geq p \\ p + (q-1)N_e - q(q-1)/2, & \text{if } q < p. \end{cases} \quad (14)$$

The number of descriptors per atom is thus  $N_{2b}N_e(N_e + 1)/2$ .



It is important to note that the orthogonal basis functions defined in (11) do not depend on the atomic numbers  $Z_i$  and  $Z_j$ . Therefore, the cost of evaluating the basis functions and their derivatives with respect to  $r_{ij}$  is independent of the number of elements  $N_e$ . Consequently, even though the two-body proper orthogonal descriptors defined in (13) depend on  $\mathbf{Z}$ , their computational complexity is independent of  $N_e$ . The computational complexity of the two-body PODs will be discussed in more detail later.

#### 2.4. Three-body proper orthogonal descriptors

In order to provide proper orthogonal descriptors for three-body interactions, we need to introduce a three-body parametrized potential. In particular, the three-body potential is defined as a product of radial and angular functions as follows

$$W^{(3)}(r_{ij}, r_{ik}, \theta_{ijk}, \boldsymbol{\eta}, \boldsymbol{\mu}^{(3)}) = \psi(r_{ij}, r_{\min}, r_{\max}, \alpha, \beta, \gamma, \kappa) f_c(r_{ij}, r_{\min}, r_{\max}) \\ \psi(r_{ik}, r_{\min}, r_{\max}, \alpha, \beta, \gamma, \kappa) f_c(r_{ik}, r_{\min}, r_{\max}) \cos(\sigma\theta_{ijk} + \zeta) \quad (15)$$

where  $\sigma$  is the periodic multiplicity,  $\zeta$  is the equilibrium angle,  $\boldsymbol{\mu}^{(3)} = (\alpha, \beta, \gamma, \kappa, \sigma, \zeta)$ . The three-body potential (15) provides an angular fingerprint of the atomic environment through the bond angles  $\theta_{ijk}$  formed with each pair of neighbors  $j$  and  $k$ . Compared to the two-body potential (8), the three-body potential (15) has two extra parameters ( $\sigma, \zeta$ ) associated with the angular component.

Let  $\boldsymbol{\varrho} = (\alpha, \beta, \gamma, \kappa)$ . We assume that we are given  $L_r$  parameter tuples  $\boldsymbol{\varrho}_\ell, 1 \leq \ell \leq L_r$ . We introduce the following set of snapshots on  $(r_{\min}, r_{\max})$ :

$$\zeta_\ell(r_{ij}, r_{\min}, r_{\max}) = \psi(r_{ij}, r_{\min}, r_{\max}, \boldsymbol{\varrho}_\ell) f_c(r_{ij}, r_{\min}, r_{\max}), \quad 1 \leq \ell \leq L_r. \quad (16)$$

We apply the Karhunen-Loève (KL) expansion to this set of snapshots to obtain orthogonal basis functions as follows

$$U_m^r(r_{ij}, r_{\min}, r_{\max}) = \sum_{\ell=1}^{L_r} A_{\ell m}^r \zeta_\ell(r_{ij}, r_{\min}, r_{\max}), \quad m = 1, \dots, N_r, \quad (17)$$

where the matrix  $\mathbf{A}^r \in \mathbb{R}^{L_r \times L_r}$  consists of eigenvectors of the eigenvalue problem which is formed similarly to (12). For the parametrized angular function, we consider angular basis functions

$$U_n^a(\theta_{ijk}) = \cos((n-1)\theta_{ijk}), \quad n = 1, \dots, N_a, \quad (18)$$

where  $N_a$  is the number of angular basis functions. The orthogonal basis functions for the parametrized potential (15) are computed as follows

$$U_{mn}^{(3)}(r_{ij}, r_{ik}, \theta_{ijk}, \boldsymbol{\eta}) = U_m^r(r_{ij}, \boldsymbol{\eta}) U_m^r(r_{ik}, \boldsymbol{\eta}) U_n^a(\theta_{ijk}), \quad (19)$$

for  $1 \leq m \leq N_r, 1 \leq n \leq N_a$ . The number of three-body orthogonal basis functions is equal to  $N_{3b} = N_r N_a$  and independent of the number of elements. Furthermore, since the basis functions do not depend on  $\mathbf{Z}$ , their computational cost is independent of the number of elements in the system.

Finally, the three-body proper orthogonal descriptors at each atom  $i$  are obtained by summing (19) over the neighbors  $j$  and  $k$  of atom  $i$  as

$$D_{imn\ell(p,q,s)}^{(3)}(\boldsymbol{\eta}) = \begin{cases} \sum_{\{j|Z_j=q\}} \sum_{\{k|Z_k=s\}} U_{mn}^{(3)}(r_{ij}, r_{ik}, \theta_{ijk}, \boldsymbol{\eta}), & \text{if } Z_i = p \\ 0, & \text{if } Z_i \neq p \end{cases} \quad (20)$$

for  $1 \leq i \leq N, 1 \leq m \leq N_r, 1 \leq n \leq N_a, 1 \leq q, p, s \leq N_e$ , where

$$\ell(p, q, s) = \begin{cases} s + (q - 1)N_e - q(q - 1)/2 + (p - 1)N_e(1 + N_e)/2, & \text{if } s \geq q \\ q + (s - 1)N_e - s(s - 1)/2 + (p - 1)N_e(1 + N_e)/2, & \text{if } s < q. \end{cases} \quad (21)$$

The number of three-body descriptors per atom is thus  $N_{3b} N_e^2 (N_e + 1)/2$ . While the number of three-body PODs increases cubically as a function of the number of elements, the computational complexity of the three-body PODs is independent of the number of elements, as we discuss below.

### 2.5. Computational complexity of proper orthogonal descriptors

We begin with analyzing the computational complexity of the two-body PODs and their derivatives with respect to  $r_{ij}$ . To this end, it follows from (11) and (13) that

$$\frac{\partial D_{iml(p,q)}^{(2)}(\boldsymbol{\eta})}{\partial r_{ij}} = \begin{cases} \frac{\partial U_m^{(2)}(r_{ij}, \boldsymbol{\eta})}{\partial r_{ij}}, & \text{if } Z_i = p, Z_j = q \\ 0, & \text{otherwise} \end{cases} \quad (22)$$

where

$$\frac{\partial U_m^{(2)}(r_{ij}, \boldsymbol{\eta})}{\partial r_{ij}} = \sum_{\ell=1}^{N_s} A_{\ell m}(\boldsymbol{\eta}) \frac{\partial \xi_{\ell}(r_{ij}, \boldsymbol{\eta})}{\partial r_{ij}}, \quad m = 1, \dots, N_{2b}. \quad (23)$$

For simplicity of exposition, we assume that the number of neighbors is equal to  $N_n$  for all atoms in the system. The total number of neighbors is thus  $NN_n$ . The operation count for computing the snapshots and their derivatives is  $O(NN_nN_s)$ . The operation count for computing the orthogonal basis functions in (11) and their derivatives in (23) is thus  $O(NN_nN_sN_{2b})$ . The operation count for evaluating the two-body PODs in (13) and their derivatives in (22) is  $O(NN_nN_{2b})$ . As a result, the computational complexity of the two-body PODs and their derivatives is  $O(NN_nN_sN_{2b})$ , which is independent of the number of elements.

The derivatives of the three-body basis functions in (19) are given by

$$\begin{aligned}\frac{\partial U_{mn}^{(3)}(r_{ij}, r_{ik}, \theta_{ijk}, \boldsymbol{\eta})}{\partial r_{ij}} &= \frac{\partial U_m^r(r_{ij}, \boldsymbol{\eta})}{\partial r_{ij}} U_m^r(r_{ik}, \boldsymbol{\eta}) \cos((n-1)\theta_{ijk}) \\ \frac{\partial U_{mn}^{(3)}(r_{ij}, r_{ik}, \theta_{ijk}, \boldsymbol{\eta})}{\partial r_{ik}} &= U_m^r(r_{ij}, \boldsymbol{\eta}) \frac{\partial U_m^r(r_{ik}, \boldsymbol{\eta})}{\partial r_{ik}} \cos((n-1)\theta_{ijk}), \\ \frac{\partial U_{mn}^{(3)}(r_{ij}, r_{ik}, \theta_{ijk}, \boldsymbol{\eta})}{\partial \theta_{ijk}} &= -(n-1)U_m^r(r_{ij}, \boldsymbol{\eta})U_m^r(r_{ik}, \boldsymbol{\eta}) \sin((n-1)\theta_{ijk}).\end{aligned}\tag{24}$$

The operation count for computing the three-body orthogonal basis functions in (19) and their derivatives in (24) is  $O(NN_n^2N_{3b})$ . Therefore, the computational complexity of the three-body PODs (20) and their derivatives is also  $O(NN_n^2N_{3b})$  and thus independent of the number of elements.

The overall computational complexity of the PODs is  $O(NN_n^2N_{3b})$  since the three-body PODs are considerably more expensive than the two-body PODs. While the number of PODs grows cubically with the the number of elements, the computational complexity of PODs is independent of the number of elements. This is in contrast to multi-element SNAP and ACE descriptors that have  $N_e$ -dependent computational complexity. For instance, the computational complexity of the multi-element SNAP descriptors [30] increases as  $O(N_e^2)$ , while that of the multi-element ACE descriptors [9] also grows with the number of elements depending on the body order of the ACE descriptors.

As the proper orthogonal descriptors are invariant with respect to translation and rotation of the atomic environment, and permutation of chemically equivalent atoms in the environment, they can be used to construct interatomic potentials. In the next section, we show that two different interatomic potentials can be constructed by combining the proper orthogonal descriptors in two different ways.

### 3. Proper Orthogonal Descriptor Potentials

In this section, we introduce two different POD potentials for multi-element systems. The first POD potential is constructed by combining the POD descriptors described in the previous section with the least-squares regression. To develop the second POD potential, we extend the original proper orthogonal descriptors to define a new set of descriptors that can capture higher-order interactions beyond three-body interaction.

#### 3.1. The first POD potential

The proper orthogonal descriptors are used to define the atomic energies in the following expansion

$$E_i(\boldsymbol{\eta}) = \sum_{p=1}^{N_e} c_p^{(1)} D_{ip}^{(1)} + \sum_{m=1}^{N_{2b}} \sum_{l=1}^{N_e(N_e+1)/2} c_{ml}^{(2)} D_{iml}^{(2)}(\boldsymbol{\eta}) + \sum_{m=1}^{N_r} \sum_{n=1}^{N_a} \sum_{\ell=1}^{N_e^2(N_e+1)/2} c_{mn\ell}^{(3)} D_{imn\ell}^{(3)}(\boldsymbol{\eta}), \quad 1 \leq i \leq N, \quad (25)$$

where  $D_{ip}^{(1)}$ ,  $D_{iml}^{(2)}$ ,  $D_{imn\ell}^{(3)}$  are the one-body, two-body descriptors, respectively, and  $c_p^{(1)}$ ,  $c_{ml}^{(2)}$ ,  $c_{mn\ell}^{(3)}$  are their respective expansion coefficients. In a more compact notation that implies summation over descriptor indices the atomic energies in (25) can be written as

$$E_i(\boldsymbol{\eta}) = \sum_{p=1}^{N_e} c_p^{(1)} D_{ip}^{(1)} + \sum_{k=1}^{N_d^{(2)}} c_k^{(2)} D_{ik}^{(2)} + \sum_{m=1}^{N_d^{(3)}} c_m^{(3)} D_{im}^{(3)} \quad (26)$$

where  $N_d^{(2)} = N_{2b} N_e (N_e + 1) / 2$  and  $N_d^{(3)} = N_{3b} N_e^2 (N_e + 1) / 2$  are the number of two-body and three-body descriptors, respectively.

The potential energy is then obtained by summing local atomic energies  $E_i$  for all atoms  $i$  in the system

$$E(\boldsymbol{\eta}) = \sum_i^N E_i(\boldsymbol{\eta}). \quad (27)$$

Because the descriptors are one-body, two-body, and three-body terms, the resulting POD potential (27) is a three-body PES. By inserting (26) into

(27), we express the potential energy as a linear combination of the global descriptors as follows

$$E(\boldsymbol{\eta}) = \sum_{p=1}^{N_e} c_p^{(1)} d_p^{(1)} + \sum_{k=1}^{N_d^{(2)}} c_k^{(2)} d_k^{(2)} + \sum_{m=1}^{N_d^{(3)}} c_m^{(3)} d_m^{(3)} \quad (28)$$

where the global descriptors are given by

$$d_p^{(1)}(\boldsymbol{\eta}) = \sum_{i=1}^N D_{ip}^{(1)}(\boldsymbol{\eta}), \quad d_k^{(2)}(\boldsymbol{\eta}) = \sum_{i=1}^N D_{ik}^{(2)}(\boldsymbol{\eta}), \quad d_m^{(3)}(\boldsymbol{\eta}) = \sum_{i=1}^N D_{im}^{(3)}(\boldsymbol{\eta}). \quad (29)$$

Hence, we obtain the atomic forces as

$$\mathbf{F} = -\nabla E(\boldsymbol{\eta}) = -\sum_{k=1}^{N_d^{(2)}} c_k^{(2)} \nabla d_k^{(2)} - \sum_{m=1}^{N_d^{(3)}} c_m^{(3)} \nabla d_m^{(3)} \quad (30)$$

where  $\nabla d_k^{(2)}$  and  $\nabla d_m^{(3)}$  are derivatives of the two-body and three-body global descriptors with respect to atom positions, respectively. Note that since the first-body global descriptors are constant, their derivatives are zero.

In actual implementation, we calculate the potential energy and atomic forces without computing and storing the per-atom and global descriptors as follows. To this end, we note from (4), (13) (20), and (25) that the atomic energies can be expressed in terms of the orthogonal basis functions as

$$E_i(\boldsymbol{\eta}) = c_{Z_i}^{(1)} + \sum_j \sum_{m=1}^{N_{2b}} c_{ml(Z_i, Z_j)}^{(2)} U_m^{(2)}(r_{ij}, \boldsymbol{\eta}) + \sum_j \sum_k \sum_{m=1}^{N_r} \sum_{n=1}^{N_a} c_{mn\ell(Z_i, Z_j, Z_k)}^{(3)} U_{mn}^{(3)}(r_{ij}, r_{ik}, \theta_{ijk}, \boldsymbol{\eta}), \quad (31)$$

where  $l(Z_i, Z_j)$  and  $\ell(Z_i, Z_j, Z_k)$  are the index mappings defined in (14) and (21), respectively. Hence, the operation count for evaluating the atomic energies and the potential energy is  $O(NN_n^2N_{3b})$ . In order to calculate the atomic forces, we need to compute the derivatives of the atomic energies  $E_i(\boldsymbol{\eta})$  with respect to  $r_{ij}$ ,  $r_{ik}$ , and  $\theta_{ijk}$ . This requires us to compute the derivatives of the orthogonal basis functions in (23) and (24) with the same operation count of  $O(NN_n^2N_{3b})$  as discussed in the previous section.

In summary, the computational complexity of the first POD potential is  $O(NN_n^2N_{3b})$ . This complexity is linear in the number of atoms and the number of three-body basis functions, quadratic in the number of neighbors, and yet independent of the number of elements. In contrast, other ML potentials such as multi-element SNAP potential [30] and ACE potential [9] have the computational complexity dependent on the number of elements.

### 3.2. The second POD potential

The first POD potential is a three-body potential because it is constructed from a set of one-body, two-body, and three-body descriptors. For many applications, it is desirable to capture higher-order interactions beyond three-body interaction. To this end, we extend the proper orthogonal descriptors described in Section 2 by coupling them to produce higher-body descriptors.

We recall two-body PODs  $D_{ik}^{(2)}, 1 \leq k \leq N_d^{(2)}$ , and three-body PODs  $D_{im}^{(3)}, 1 \leq m \leq N_d^{(3)}$ , with  $N_d^{(2)} = N_{2b}N_e(N_e + 1)/2$  and  $N_d^{(3)} = N_{3b}N_e^2(N_e + 1)/2$  being the number of descriptors per atom for the two-body PODs and three-body PODs, respectively. We employ them to define a new set of atomic descriptors as follows

$$D_{ikm}^{(2*3)} = \frac{1}{2N} \left( D_{ik}^{(2)} \sum_{j=1}^N D_{jm}^{(3)} + D_{im}^{(3)} \sum_{j=1}^N D_{jk}^{(2)} \right) \quad (32)$$

for  $1 \leq i \leq N, 1 \leq k \leq N_d^{(2)}, 1 \leq m \leq N_d^{(3)}$ . The new descriptors are four-body because they involve central atom  $i$  together with three neighbors  $j, k$  and  $l$ . The number of new descriptors per atom is equal to

$$N_d^{(2*3)} = N_d^{(2)} * N_d^{(3)} = N_{2b}N_{3b}N_e^3(N_e + 1)^2/4. \quad (33)$$

The new global descriptors are calculated as

$$d_{km}^{(2*3)} = \sum_{i=1}^N D_{ikm}^{(2*3)} = \left( \sum_{i=1}^N D_{ik}^{(2)} \right) \left( \sum_{i=1}^N D_{im}^{(3)} \right) = d_k^{(2)} d_m^{(3)}, \quad (34)$$

for  $1 \leq k \leq N_d^{(2)}, 1 \leq m \leq N_d^{(3)}$ . Hence, the gradient of the new global descriptors with respect to atom positions is calculated as

$$\nabla d_{km}^{(2*3)} = d_m^{(3)} \nabla d_k^{(2)} + d_k^{(2)} \nabla d_m^{(3)}, \quad 1 \leq k \leq N_d^{(2)}, 1 \leq m \leq N_d^{(3)}. \quad (35)$$

It is also possible to combine the three-body descriptors with the same three-body descriptors (instead of the two-body ones) to produce a new set of five-body descriptors.

The second POD potential is defined as a linear combination of the original and new global descriptors as follows

$$E = \sum_{p=1}^{N_e} c_p^{(1)} d_p^{(1)} + \sum_{k=1}^{N_d^{(2)}} c_k^{(2)} d_k^{(2)} + \sum_{m=1}^{N_d^{(3)}} c_m^{(3)} d_m^{(3)} + \sum_{k=1}^{N_d^{(2)}} \sum_{m=1}^{N_d^{(3)}} c_{km}^{(2*3)} d_{km}^{(2*3)}. \quad (36)$$

It follows from (34) and (36) that

$$\begin{aligned} E = & \sum_{p=1}^{N_e} c_p^{(1)} d_p^{(1)} + \sum_{k=1}^{N_d^{(2)}} \left( c_k^{(2)} + 0.5 \sum_{m=1}^{N_d^{(3)}} c_{km}^{(2*3)} d_m^{(3)} \right) d_k^{(2)} + \\ & \sum_{m=1}^{N_d^{(3)}} \left( c_m^{(3)} + 0.5 \sum_{k=1}^{N_d^{(2)}} c_{km}^{(2*3)} d_k^{(2)} \right) d_m^{(3)}, \end{aligned} \quad (37)$$

which is simplified to

$$E = \sum_{p=1}^{N_e} c_p^{(1)} d_p^{(1)} + \sum_{k=1}^{N_d^{(2)}} \left( c_k^{(2)} + 0.5 b_k^{(2)} \right) d_k^{(2)} + \sum_{m=1}^{N_d^{(3)}} \left( c_m^{(3)} + 0.5 b_m^{(3)} \right) d_m^{(3)}, \quad (38)$$

where

$$\begin{aligned} b_k^{(2)} &= \sum_{m=1}^{N_d^{(3)}} c_{km}^{(2*3)} d_m^{(3)}, \quad k = 1, \dots, N_d^{(2)}, \\ b_m^{(3)} &= \sum_{k=1}^{N_d^{(2)}} c_{km}^{(2*3)} d_k^{(2)}, \quad m = 1, \dots, N_d^{(3)}. \end{aligned} \quad (39)$$

We see that the expression of the potential energy (38) for the second POD potential is similar to (28) for the first POD potential except for the extra evaluation of  $b_k^{(2)}$  and  $b_m^{(3)}$  in (39).

Next, we describe force calculation for the second POD potential (36) resulting in the following atomic forces

$$\mathbf{F} = - \sum_{k=1}^{N_d^{(2)}} c_k^{(2)} \nabla d_k^{(2)} - \sum_{m=1}^{N_d^{(3)}} c_m^{(3)} \nabla d_m^{(3)} - \sum_{k=1}^{N_d^{(2)}} \sum_{m=1}^{N_d^{(3)}} c_{km}^{(2*3)} \nabla d_{km}^{(2*3)}. \quad (40)$$

It follows from (35) and (39) that

$$\begin{aligned}
\sum_{k=1}^{N_d^{(2)}} \sum_{m=1}^{N_d^{(3)}} c_{km}^{(2*3)} \nabla d_{km}^{(2*3)} &= \sum_{k=1}^{N_d^{(2)}} \sum_{m=1}^{N_d^{(3)}} c_{km}^{(2*3)} (d_m^{(3)} \nabla d_k^{(2)} + d_k^{(2)} \nabla d_m^{(3)}) \\
&= \sum_{k=1}^{N_d^{(2)}} \left( \sum_{m=1}^{N_d^{(3)}} c_{km}^{(2*3)} d_m^{(3)} \right) \nabla d_k^{(2)} + \sum_{m=1}^{N_d^{(3)}} \left( \sum_{k=1}^{N_d^{(2)}} c_{km}^{(2*3)} d_k^{(2)} \right) \nabla d_m^{(3)} \\
&= \sum_{k=1}^{N_d^{(2)}} b_k^{(2)} \nabla d_k^{(2)} + \sum_{m=1}^{N_d^{(3)}} b_m^{(3)} \nabla d_m^{(3)}.
\end{aligned}$$

It follows from this equation and (40) that we obtain

$$\mathbf{F} = - \sum_{k=1}^{N_d^{(2)}} \left( c_k^{(2)} + b_k^{(2)} \right) \nabla d_k^{(2)} - \sum_{m=1}^{N_d^{(3)}} \left( c_m^{(3)} + b_m^{(3)} \right) \nabla d_m^{(3)}. \quad (41)$$

We see again that the expression for the atomic forces of the second POD potential is similar to (30) of the first POD potential except for the extra calculation of  $b_k^{(2)}$  and  $b_m^{(3)}$ .

To calculate  $b_k^{(2)}$  and  $b_m^{(3)}$  in (39), we must compute the two-body and three-body global descriptors as follows

$$\begin{aligned}
d_{ml(p,q)}^{(2)}(\boldsymbol{\eta}) &= \sum_{\{i|Z_i=p\}} \sum_{\{j|Z_j=q\}} U_m^{(2)}(r_{ij}, \boldsymbol{\eta}) \\
d_{mn\ell(p,q,s)}^{(3)}(\boldsymbol{\eta}) &= \sum_{\{i|Z_i=p\}} \sum_{\{j|Z_j=q\}} \sum_{\{k|Z_k=s\}} U_{mn}^{(3)}(r_{ij}, r_{ik}, \theta_{ijk}, \boldsymbol{\eta}).
\end{aligned} \quad (42)$$

Since the double and triple sums are performed for all the orthogonal basis functions, the operation count for computing the global descriptors in (42) is  $O(NN_n^2N_{3b})$ . Note that the operation count for calculating  $b_k^{(2)}$  and  $b_m^{(3)}$  in (39) is  $O(N_d^2N_d^3)$  and thus negligible when it is compared to that for computing the global descriptors in (42).

In summary, the computational complexity of the second POD potential is  $O(NN_n^2N_{3b})$ , which is exactly the same as that of the first POD potential. As the body order of the second POD potential is higher than the first potential, it can represent the potential energy surface more accurately. For



the remainder of this paper, the first POD potential is referred to as the linear POD potential, while the second POD potential as the quadratic POD potential. It is straightforward to construct another quadratic POD potential by coupling the three-body descriptors with themselves.

### 3.3. Relation to the quadratic SNAP potential

A crucial aspect of ML potentials is the composition of the descriptors by using a variety of linear and nonlinear forms as well as different regression methods. The simplest composition is a linear combination of the descriptors and leads to linear potentials [16]. While the linear composition of descriptors is extremely efficient to develop potentials, it may limit the accuracy of the resulting potential. A quadratic composition of the SNAP descriptors was proposed in [17] and shown to increase accuracy relative to the linear SNAP potential. The quadratic POD potential bears similarities and differences with the quadratic SNAP potential [17] as discussed below.

The main idea of the quadratic SNAP is to make new quadratic descriptors from the original descriptors as follows

$$D_{ikm}^{(2*3)} = D_{ik}^{(2)} D_{im}^{(3)}, \quad k = 1, \dots, N_d^{(2)}, m = 1, \dots, N_d^{(3)}. \quad (43)$$

The associated global descriptors are thus calculated as

$$d_{km}^{(2*3)} = \sum_{i=1}^N D_{ikm}^{(2*3)} = \sum_{i=1}^N D_{ik}^{(2)} D_{im}^{(3)}. \quad (44)$$

We see that the new global descriptors of the quadratic SNAP potential cannot be expressed the products of the original global descriptors, whereas those of the quadratic POD potential can be as shown by (34). As a result, the quadratic SNAP potential cannot be written as a linear combination of the original global descriptors, whereas the quadratic POD potential can be as shown by (38). The quadratic SNAP potential is more expensive than the linear SNAP potential because evaluating the quadratic terms and their derivatives for force calculation incurs a significant increase in computational cost and memory storage. As discussed earlier, the quadratic POD potential has the same computational complexity as the linear POD potential.

## 4. Potential Fitting

### 4.1. Weighted least-squares regression

ML potentials must be trained using reference data in order to construct a model that composes the descriptors to form the PES. The reference data

are often obtained by using *ab initio* methods for self-consistent calculation of the electronic structures. With the availability of high-performance computers and highly optimized density functional theory (DFT) codes, it is not difficult to generate DFT data for many thousands of configurations to fit ML potentials. There are many different methods that can be used to construct the ML model such as least-squares regression, neural networks, graph neural networks, Gaussian processes regression, and support vector machine. The least-squares regression is used here because it is the simplest and most efficient method, although it is not the most accurate method.

Let  $J$  be the number of training configurations, with  $N_j$  being the number of atoms in the  $j$ th configuration. Let  $\{E_j^*\}_{j=1}^J$  and  $\{\mathbf{F}_j^*\}_{j=1}^J$  be the DFT energies and forces for  $J$  configurations. Next, we calculate the global descriptors and their derivatives for all training configurations. Let  $d_{jm}$ ,  $1 \leq m \leq M$ , be the global descriptors associated with the  $j$ th configuration, where  $M$  is the number of global descriptors. We then form a matrix  $\mathbf{A} \in \mathbb{R}^{J \times M}$  with entries  $A_{jm} = d_{jm}/N_j$  for  $j = 1, \dots, J$  and  $m = 1, \dots, M$ . Moreover, we form a matrix  $\mathbf{B} \in \mathbb{R}^{\mathcal{N} \times M}$  by stacking the derivatives of the global descriptors for all training configurations from top to bottom, where  $\mathcal{N} = 3 \sum_{j=1}^J N_j$ .

The coefficient vector  $\mathbf{c}$  of the linear expansion (26) is found by solving the following least-squares problem

$$\min_{\mathbf{c} \in \mathbb{R}^M} \beta \|\mathbf{A}(\boldsymbol{\eta})\mathbf{c} - \bar{\mathbf{E}}^*\|^2 + \|\mathbf{B}(\boldsymbol{\eta})\mathbf{c} + \mathbf{F}^*\|^2, \quad (45)$$

where  $\beta$  is a scalar to weight the energy contribution. Here  $\bar{\mathbf{E}}^* \in \mathbb{R}^J$  is a vector of with entries  $\bar{E}_j^* = E_j^*/N_j$  and  $\mathbf{F}^*$  is a vector of  $\mathcal{N}$  entries obtained by stacking  $\{\mathbf{F}_j^*\}_{j=1}^J$  from top to bottom.

The training procedure is the same for both the first and second POD potentials. However, since the second POD potential has a significantly larger number of the global descriptors, it is considerably more expensive the first POD potential in terms of the computational cost and memory storage. This is because the fitting of the second POD potential still requires us to calculate and store the new global descriptors in (34) and their gradient in (35). Furthermore, the second POD potential may require more training data in order to prevent overfitting. In order to reduce the computational cost of fitting the second POD potential and avoid overfitting, we can use subsets of two-body and three-body PODs for constructing the new descriptors.

#### 4.2. Optimization of hyperparameters

The hyperparameters contain inner and outer cut-off distances for two-body and three-body interactions. They can affect the prediction performance of the resulting potential. We observe through our numerical experiences that longer cut-off distances do not necessarily translate to better performance. Furthermore, setting them to some heuristic values may lead to an interatomic potential that can be less accurate than the potential obtained by optimizing the cut-off distances. Therefore, it is necessary to optimize the hyperparameters.

Let  $\Omega^\eta$  be a domain in which the hyperparameters reside. We consider solving the following constrained optimization problem

$$\begin{aligned} \min_{\boldsymbol{\eta} \in \Omega^\eta, \mathbf{c} \in \mathbb{R}^M} & w \|\mathbf{A}(\boldsymbol{\eta})\mathbf{c}(\boldsymbol{\eta}) - \bar{\mathbf{E}}^*\|_{\text{MAE}} + (1 - w) \|\mathbf{B}(\boldsymbol{\eta})\mathbf{c}(\boldsymbol{\eta}) - \mathbf{F}^*\|_{\text{MAE}} \\ \text{subject to } & (\beta^2 \mathbf{A}^T \mathbf{A} + \mathbf{B}^T \mathbf{B})\mathbf{c} = (\beta^2 \mathbf{A}^T \bar{\mathbf{E}}^* + \mathbf{B}^T \mathbf{F}^*) \end{aligned} \quad (46)$$

where  $w \in [0, 1]$  is a given scalar weight, and  $\|\cdot\|_{\text{MAE}}$  is defined as

$$\|\mathbf{e}\|_{\text{MAE}} = \frac{1}{n} \sum |e_i|. \quad (47)$$

Note that the equality constraint in (46) is obtained from the optimality condition of the least-squares problem (45).

The optimization problem (46) is generally nonlinear and non-convex. Instead of directly solving the problem (46), we solve a surrogate problem. To this end, we approximate the loss function in (46) using polynomial tensor-product interpolation. In particular, we divide the domain  $\Omega^\eta$  into  $Q$  grid points  $\{\boldsymbol{\eta}_q\}_{q=1}^Q$  and compute the loss function at those grid points. This requires us to solve the linear system in the constraint of the problem (46)  $Q$  times for  $\boldsymbol{\eta} = \boldsymbol{\eta}_q, q = 1, \dots, Q$ . We then fit the loss values at the grid points to a tensor-product multivariate polynomial of certain degree to construct a surrogate model of the loss function. Finally, the gradient descent algorithm is used to minimize the surrogate model to obtain the hyperparameters. In order to be able to reach the global minimum, we start our gradient descent algorithm with a large number of initial guesses randomly sampled in  $\Omega^\eta$ .

### 5. Numerical Experiments

In this section, we assess the performance of POD potentials for indium phosphide and titanium dioxide. The linear POD potential in Section 3.1

and the quadratic POD potential in Section 3.2 shall be referred to as POD-I and POD-II, respectively. In addition, we present results with the ACE potential [9] and the explicit multi-element SNAP (EME-SNAP) potential [30]. We fit EME-SNAP potential with the FitSNAP package, ACE potential with the ACE1 package, and POD potentials with ML-POD package available in LAMMPS [31]. POD potentials are available on Github (<https://github.com/cesmix-mit/pod-examples>) to facilitate the reproduction of our work. For POD and ACE potentials, the optimization problem (46) is solved with  $\beta = 100$  and  $w = 0.8$ . For EME-SNAP potentials, we use the original EME-SNAP potential in [30] for different values of  $J$ .

### 5.1. Indium phosphide

In the paper [30], Cusentino et. al introduced an explicit multi-element SNAP potential and demonstrated it for indium phosphide (InP) dataset generated using the Vienna Ab Initio Simulation Package (VASP). The InP dataset contains not only chemically unique environment but also high-energy defects which are intended to study radiation damage effects where collision cascades of sufficiently high energy leave behind high formation energy point defects. In addition to defect configurations, the dataset includes configurations for uniform expansion and compression (Equation of State), random cell shape modifications (Shear group), and uniaxially strained (Strain group) unit cells for zincblende crystal structure. In total, the dataset has 1894 configurations with atom counts per configuration ranging from 8 to 216. In [30], the training energy and force errors for EME-SNAP potential are reported as 3.3 meV/atom and 67 meV/Å, respectively.

Table 1 provides the optimized cutoff distances and the number of descriptors for different values of the number of basis functions  $N_f$ . For POD potentials, the number of basis functions is defined as the sum of the two-body and three-body basis functions  $N_f = N_{2b} + N_{3b}$ . For both ACE and EME-SNAP, the number of basis functions  $N_f$  is defined as the number of bispectrum components per atom for one-element systems. For EME-SNAP, the number of basis functions is related to  $J$  as  $N_f = (J+1)(J+2)(J+3/2)/3$ . Note that the number of descriptors for EME-SNAP is  $N_d = N_f N_e^4$ . POD-I has the smallest number of descriptors, whereas POD-II has the largest number of descriptors. EME-SNAP has more number of descriptors than ACE. For POD-I, POD-II potentials, the cutoff distances tend to increase with  $N_f$ . Figure 1 show the polynomial interpolation surrogate of the loss function for POD-I at  $N_f = 30$ . We see that the surrogate loss function is smooth with

multiple local minima. The global minimum ( $r_{\min} = 0.56, r_{\max} = 4.37$ ) is indicated by the red circle in Figure 1. We see that cutoff distances affect the value of the loss function and thus the accuracy of the resulting potential. Therefore, it is beneficial to optimize these hyperparameters.

	<b>ACE</b>				<b>POD-I</b>			<b>POD-II</b>			<b>EME-SNAP</b>	
$N_f$	$N_d$	$r_{\min}$	$r_{\max}$		$N_d$	$r_{\min}$	$r_{\max}$	$N_d$	$r_{\min}$	$r_{\max}$	$N_d$	$J$
5	26	0.30	5.00		26	0.30	4.25	134	0.38	4.69	80	2
14	108	1.13	5.00		83	0.31	4.43	731	0.59	4.63	224	4
30	246	1.24	4.91		170	0.56	4.37	2870	0.50	4.76	480	6
55	506	1.41	4.91		314	0.36	4.80	7226	0.62	4.81	880	8
91	870	1.41	4.91		515	0.65	4.93	16355	0.72	4.91	1456	10

Table 1: The optimized cutoff distances  $r_{\min}$  and  $r_{\max}$ , and number of descriptors  $N_d$  for different values of  $N_f$  for ACE, POD-I, and POD-II. For EME-SNAP potentials, we use the original EME-SNAP potential in [30] for  $J = 2, 4, 6, 8, 10$ .

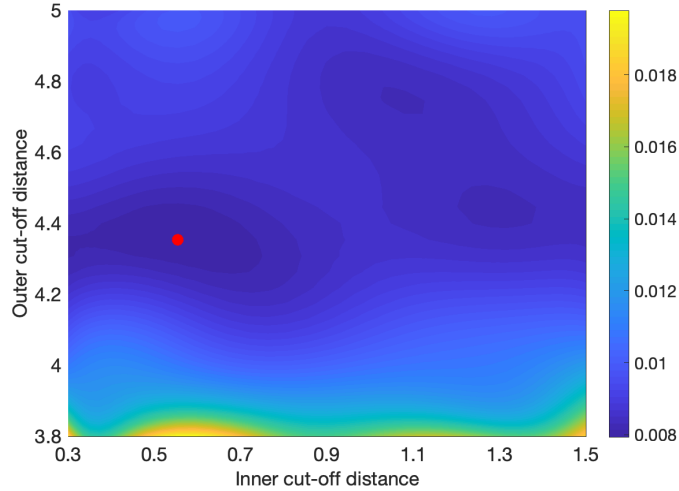


Figure 1: Surrogate loss function of the POD-I potential as a function of inner and outer cutoff distances for  $N_f = 30$ . The red circle indicates the optimal value of the cutoff distances for which the surrogate loss function is minimum

Figure 2 depicts training errors in energies and forces predicted using ACE, EME-SNAP, POD potentials for different values of the number of the basis functions. We observe convergence of the energy and force errors as the number of basis functions increases. Therefore, the errors are correlated to

the number of basis functions. POD-I, ACE, and EME-SNAP yield similar energy errors. EME-SNAP has larger force errors than POD-I and ACE except for  $N_f = 91$  where they have similar energy and force errors. For  $N_f = 30$ , the mean absolute errors are about 2.30 meV/atom and 22.33 meV/Å for ACE, 3.31 meV/atom and 67.52 meV/Å for EME-SNAP, 2.80 meV/atom and 25.82 meV/Å for POD-I, and 0.37 meV/atom and 7.07 meV/Å for POD-II. For  $N_f = 91$ , the errors are about 0.87 meV/atom and 21.61 meV/Å for ACE, 0.58 meV/atom and 20.22 meV/Å for EME-SNAP, 1.01 meV/atom and 15.10 meV/Å for POD-I, and 0.07 meV/atom and 2.28 meV/Å for POD-II. POD-II has significantly lower errors than the other potentials. The errors for POD-II are more or less a factor of 10 smaller than those for ACE, EME-SNAP, and POD-I.

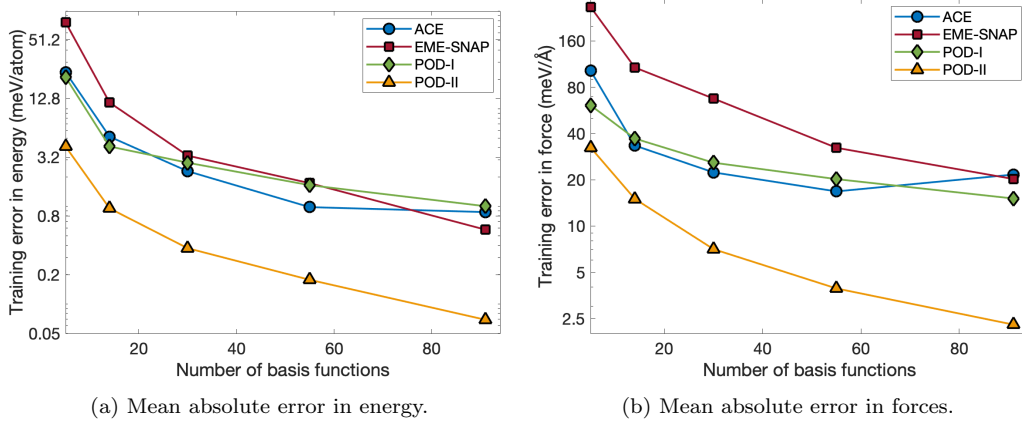


Figure 2: Training errors in energy and force as a function of the number of basis functions for ACE, POD-I, POD-II, and EME-SNAP for InP.

Figure 3 shows the trade-off between computational cost and training error for EME-SNAP, POD-I, POD-II potentials for different numbers of basis functions listed in Table 1. The computational cost is measured in terms of second per time step per atom for molecular dynamics (MD) simulations. These MD simulations are performed using LAMMPS [31] on a single CPU core of Intel i7 2.4 GHz with  $10 \times 10 \times 10$  bulk supercell containing 8000 InP atoms. We see that POD-II has almost the same computational cost as POD-I for the same number of basis functions, while having considerably lower energy errors than POD-I. This is because POD-II has exactly the same computational complexity as POD-I. Meanwhile, POD-I is many times faster than EME-SNAP for the same accuracy. In particular, POD-

I is about 9 times faster than EME-SNAP for  $N_f = 55$ , while POD-I and EME-SNAP have energy errors of 1.65 meV/atom and 1.73 meV/atom, respectively. POD-II significantly outperforms EME-SNAP in the sense that POD-II is about 54 times faster than EME-SNAP for the same accuracy of 1 meV/atom.

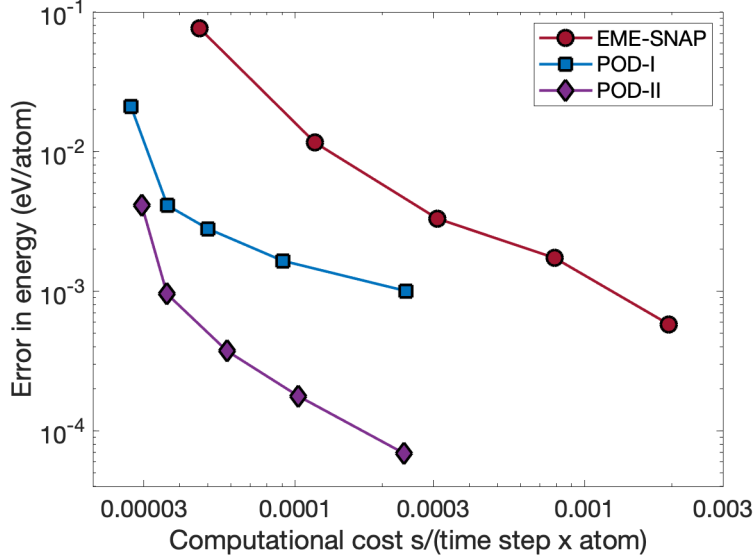


Figure 3: Training error versus the computational cost of MD simulations for the InP system of 8000 atoms. MD simulations are performed using LAMMPS [31] on a single CPU core of Intel i7 2.3 GHz for EME-SNAP, POD-I, POD-II for different numbers of basis functions listed in Table 1.

Figure 4 displays the histogram of mean absolute energy errors for all the training structures as predicted by POD-I and POD-II using  $N_f = 30$  basis functions. For POD-I, more than 50% of the structures has an energy error of less than 2 meV/atom, while 99% of the structures are predicted with an energy error of less than 10 meV/atom. For POD-II, almost all the structures are predicted with an energy error of less than 1 meV/atom, while 75% of the structures has an energy error of less than 0.2 meV/atom. Although these error statistics for energy prediction are very good, for practical purposes it is crucial that atomic forces are predicted accurately. No matter how accurate the energy prediction is, the potential is unsuitable for molecular dynamics simulations if the predicted forces are inaccurate. As shown in Figure 5, more than 95% of the structures are predicted with a force error of less than 80 meV/Å for POD-I and 20 meV/Å for POD-II. At such level of accuracy

in force prediction, POD-I is acceptable for molecular dynamics simulations, while POD-II is far superior to POD-I.

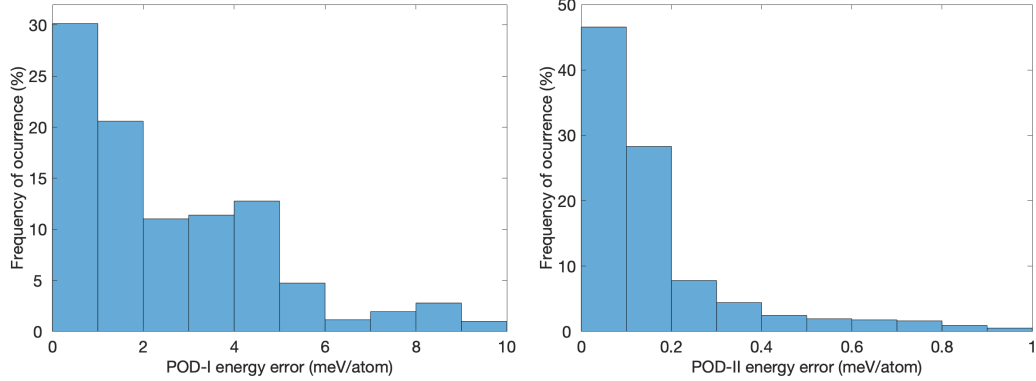


Figure 4: Histogram distribution of energy errors for all structures in the training set as predicted by POD-I (left) and POD-II (right) using  $N_f = 30$  basis functions.

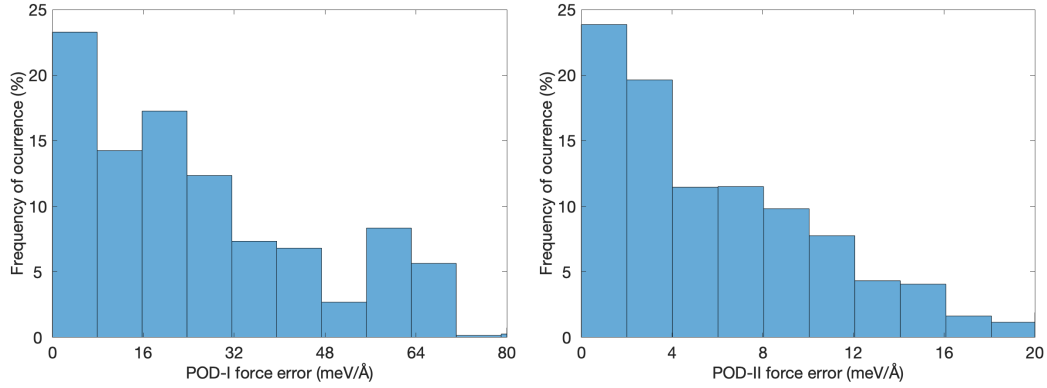


Figure 5: Histogram distribution of force errors for all structures in the training set as predicted by POD-I (left) and POD-II (right) using  $N_f = 30$  basis functions.

Table 2 provides the errors in energy and forces for five training groups. The MAE force errors for Bulk group are zero, because the bulk structure is equilibrium. Interestingly, EME-SNAP has much larger force error than the other potentials for the Shear group. Defects and Shear groups result in considerably larger force errors than the other groups. Hence, it is more difficult for interatomic potentials to predict forces for defects and random unit cells. POD-II has significantly lower energy and force errors than the other potentials for Defects and Shear groups. All the potentials predict



defect formation energies with accuracy of 1.33 meV/atom or less, which is below the limit of DFT errors. POD-II accurately reproduces DFT values of energy and force for defects, as it has 0.07 meV/atom and 2.39 meV/Å for Defects group. This level of accuracy in force prediction is extremely high and far beyond the accuracy level required by MD simulations.

<b>Group</b>		<b>ACE</b>		<b>EME-SNAP</b>		<b>POD-I</b>		<b>POD-II</b>	
Name	$N_{\text{config}}$	$\varepsilon_E$	$\varepsilon_F$	$\varepsilon_E$	$\varepsilon_F$	$\varepsilon_E$	$\varepsilon_F$	$\varepsilon_E$	$\varepsilon_F$
Bulk	1	0.51	0.00	0.01	0.00	2.18	0.00	0.91	0.00
EOS	268	1.67	0.66	1.62	0.35	1.02	0.80	0.09	0.02
Shear	346	1.02	23.16	0.92	163.68	0.19	7.98	0.03	0.75
Strain	163	1.41	0.12	0.35	0.02	1.82	0.03	0.11	0.16
Defects	1116	0.56	22.21	0.26	17.28	1.33	17.13	0.07	2.39

Table 2: MAEs in energies ( $\varepsilon_E$ ) and forces ( $\varepsilon_F$ ) for ACE, EME-SNAP, POD-I, POD-II potentials with  $N_f = 91$  for five different configuration groups of the InP compound. The units of the mean absolute errors in energies and forces are meV/atom and meV/Å, respectively.

Point defects are created when atoms become vacant at lattice sites (vacancy defect), occupy locations in the crystal structure at which there are usually not an atom (interstitial defect), or exchange positions with other atoms of different types (antisite defect). Table 3 shows the errors in energy and forces for the following point defects created from an equilibrium configuration of 64 atoms:  $\text{In}_a\text{P}_a$ ,  $\text{In}_v\text{P}_v$ ,  $\text{In}_a$ ,  $\text{P}_a$ ,  $\text{In}_i$ ,  $\text{P}_i$ ,  $\text{In}_v$ , and  $\text{P}_v$ , where subscripts correspond to vacancy(v), interstitial(i) and anti-site(a) defects. All the potentials predict these point defects very accurately. EME-SNAP predicts the vacancy defects more accurately than the other point defects. POD-II has the lowest errors for almost point defects except  $\text{In}_v$ .

In addition to defect formation energies, we also study cohesive energies for different low-energy crystal structures. Figure 6 plots the energy per atom computed with DFT, POD-I, POD-II as a function of volume per atom for the rocksalt (RS) and zincblende (ZB) crystal structures. We see that the predicted cohesive energies are very close to the DFT cohesive energies for both the rocksalt (RS) and zincblende (ZB) crystal structures. Furthermore, POD-I and POD-II correctly predict ZB as the most stable structure and reproduce the experimental cohesive energy of -3.48 eV/atom at a volume of  $24.4 \text{ Å}^3/\text{atom}$  [32]. The predicted cohesive energies for the RS structure match exactly the DFT value of -3.30 eV/atom at a volume of  $19.7 \text{ Å}^3/\text{atom}$ .

Defect Type			ACE		EME-SNAP		POD-I		POD-II	
Name	$N_{\text{atom}}$	$N_{\text{config}}$	$\varepsilon_E$	$\varepsilon_F$	$\varepsilon_E$	$\varepsilon_F$	$\varepsilon_E$	$\varepsilon_F$	$\varepsilon_E$	$\varepsilon_F$
In <sub>a</sub> P <sub>a</sub>	64	18	0.64	33.43	0.03	13.45	5.74	37.19	0.02	2.51
In <sub>v</sub> P <sub>v</sub>	62	65	1.25	36.99	0.06	8.88	3.22	40.48	0.02	3.17
In <sub>a</sub>	64	121	0.17	12.96	0.11	33.03	1.47	11.95	0.11	1.57
P <sub>a</sub>	64	72	0.47	30.56	0.82	33.33	3.10	31.56	0.07	2.27
In <sub>i</sub>	65	144	0.72	41.80	0.07	20.94	0.35	28.04	0.02	2.48
P <sub>i</sub>	65	137	0.60	32.98	0.31	19.35	0.42	22.59	0.02	2.23
In <sub>v</sub>	63	17	0.54	21.15	0.02	0.52	1.14	25.31	0.03	1.76
P <sub>v</sub>	63	77	0.34	16.47	0.04	2.54	0.42	18.25	0.03	1.61

Table 3: MAEs in energy (meV/atom) and forces (meV/Å) for different point defects for ACE, EME-SNAP, POD-I, POD-II potentials with  $N_f = 91$ . The point defects are created from an equilibrium configuration of 64 atoms by inserting atoms (interstitial defects), removing atoms (vacancy defects), or exchanging atoms of different types (antisite defects). Subscripts correspond to vacancy(v), interstitial(i) and antisite(a) point defects.

While not plotted in Figure 6, the predicted cohesive energies for the wurtzite ground state structure agree well with the DFT value of -3.45eV/atom at a volume of 25.1 Å<sup>3</sup>/atom. The potentials accurately predict the cohesive energies for the low-energy crystal structures.

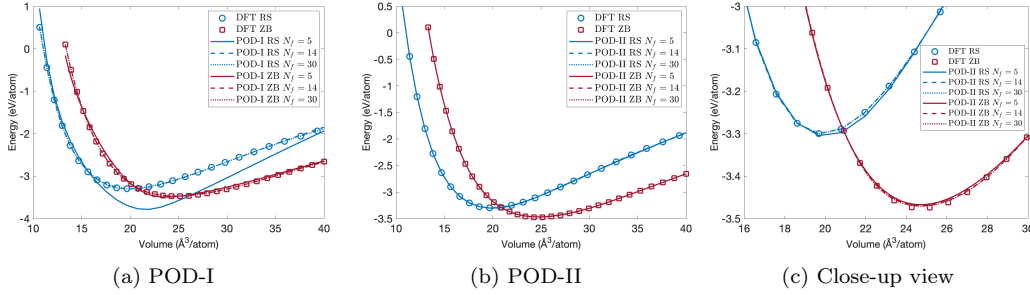


Figure 6: Energy per atom versus volume per atom for rocksalt (RS) and zincblende (ZB) crystal structures of the InP compound for POD-I and POD-II potentials. The right figure shows the close-up view of the curves near the cohesive energies.

In this study, the point defects of the InP compound were the primary focus, since accurately reproducing the defect formation energies is essential for realistic simulations of radiation damage [30]. We found that the quadratic POD potential significantly improves the accuracy of energy and force predictions when it is compared to the linear POD potential as well as ACE and EME-SNAP potentials. Specifically, it has approximately 10 smaller energy

errors and 4 times smaller force errors than the linear POD potential. We also found that all the potentials are able to accurately predict the formation energies of many different defects far beyond the chemical accuracy of DFT. Nevertheless, additional training data will be needed to improve these ML potentials for other target applications. For instance, adding liquid phase training data is useful to study melting of InP.

### 5.2. Titanium dioxide

Titanium dioxide ( $\text{TiO}_2$ ) is one of the most chemically stable, environmentally compatible, and functionally versatile metal oxides, thereby making itself an ideal compound to demonstrate interatomic potentials. Over the years, several empirical potentials have been developed for  $\text{TiO}_2$ , including rigid-ion models [33, 34], polarizable models [35, 36], ReaxFF potential [37], and COMB potential [38]. More recently, a number of neural network potentials have been constructed for  $\text{TiO}_2$ , including artificial neural network (ANN) potential [39], committee neural network (CNN) potential [40], and deep neural network (DNN) potential [41]. Herein we would like to demonstrate the performance of ACE, SNAP, and POD potentials for  $\text{TiO}_2$  on publicly available DFT data set [39].

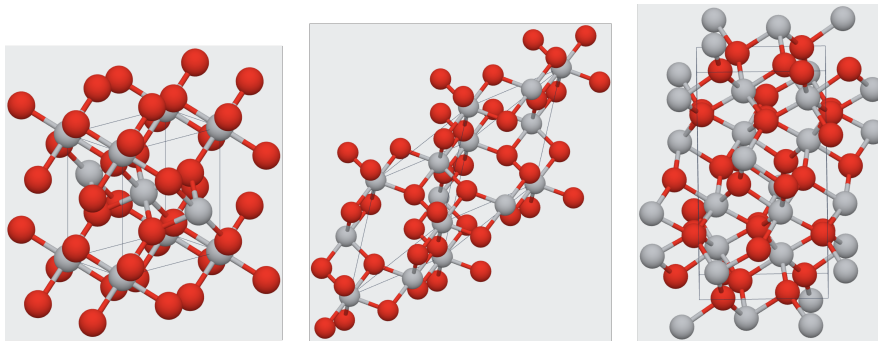


Figure 7: Unit cells of the three  $\text{TiO}_2$  polymorphs: rutile (left), anatase (middle), and (c) brookite (right). Red spheres indicate oxygen atoms and grey spheres are titanium atoms.

Natural  $\text{TiO}_2$  minerals occur in three polymorphs: rutile (tetragonal), anatase (tetragonal), and brookite (orthorhombic). The unit cells of these polymorphs are shown in Figure 7. In [39], a diverse DFT data set was generated to train an ANN potential for  $\text{TiO}_2$  using an iterative refinement method. An initial set of reference structures was generated by distorting ideal rutile, anatase, and brookite structures around the ground state. In

addition, supercell structures with oxygen vacancies were also included in the initial data set. Subsequently, additional reference structures were generated by performing short molecular dynamics simulations at various temperatures. This process was repeated until the newly generated structures were found to be accurately represented by the ANN potential. The final data set comprised a total of 7815 structures containing between 6 and 95 atoms. We refer to [39] for additional information about the DFT data set for  $\text{TiO}_2$ .

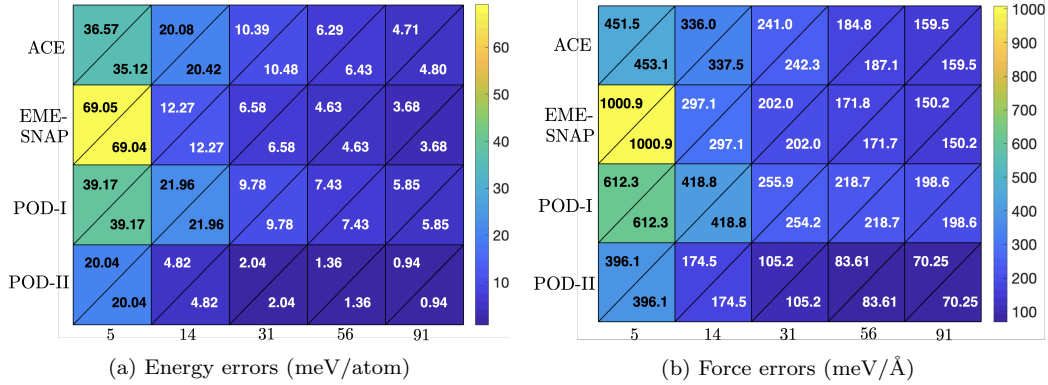


Figure 8: Mean absolute errors in energies (a) and forces (b) as a function of the number of basis functions for all four potentials for  $\text{TiO}_2$ . The upper left and lower right triangles within each cell represent training and test errors, respectively.

We use 50% of the data set (3908 training structures) to fit ACE, SNAP, and POD potentials, while employing the rest of the data set (3907 test structures) as an independent testing set to assess the accuracy of the potentials and detect overfitting. A common way to detect overfitting is to compare the accuracy of the model for test structures (test errors) to the accuracy of the model for training structures (training errors). The training and test errors are shown in Figure 8. The test errors are almost identical to the training errors for ACE, SNAP, and POD-I, POD-II potentials. The convergence of both energy and force errors is fast when  $N_f$  is less than 30. When  $N_f$  increases above 30, the convergence becomes slower. In terms of accuracy comparison, ACE is slightly more accurate than POD-I, while SNAP is more accurate than ACE. POD-II is the most accurate potential since it has the lowest energy and force errors. Indeed, POD-II with  $N_f = 30$  is even more accurate than POD-I, ACE and SNAP with  $N_f = 91$ . For  $N_f = 91$ , POD-II predicts the mean absolute errors of about 0.94 meV/atom and 70 meV/Å which are several times smaller than those predicted by the other potentials.

Figure 9 displays the histogram of mean absolute energy errors for all the test structures as predicted by POD-I and POD-II using  $N_f = 30$  basis functions. For POD-I, more than 55% of the structures has an energy error of less than 8 meV/atom, while 99% of the structures are predicted with an energy error of less than 50 meV/atom. For POD-II, almost all the structures are predicted with an energy error of less than 12 meV/atom, while 55% of the structures has an energy error of less than 2 meV/atom. The errors predicted by POD-II are several times less than those by POD-I. Hence, POD-II provides significantly more accurate prediction than POD-I while having the same computational cost.

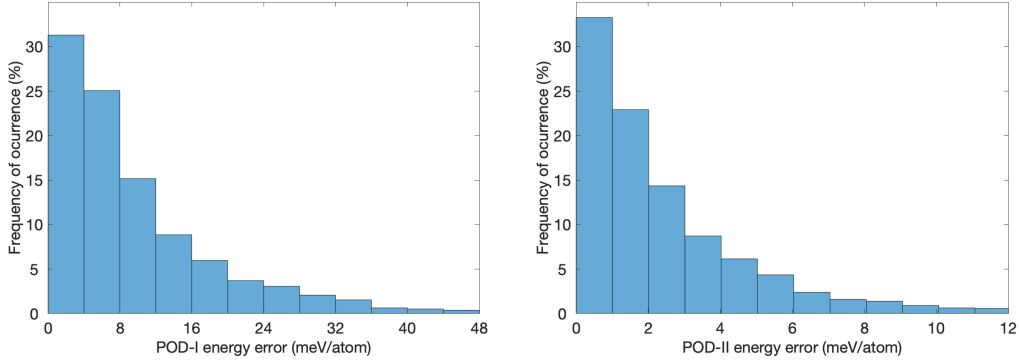


Figure 9: Histogram distribution of energy errors for all structures in the test set as predicted by POD-I (left) and POD-II (right) using  $N_f = 30$  basis functions.

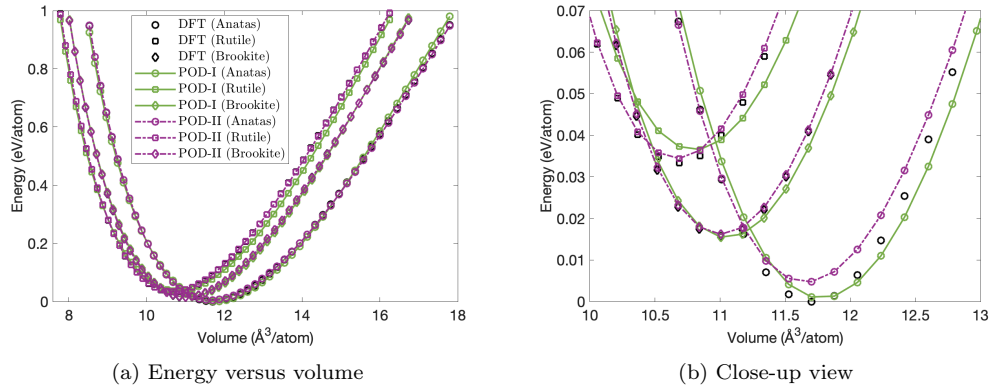


Figure 10: Energy per atom versus volume per atom for anatase, rutile, and brookite crystal structures of the  $\text{TiO}_2$  compound for DFT, and POD-I, POD-II potentials with  $N_f = 30$ . The right figure shows the close-up view of the curves near the cohesive energies.

Figure 10 plots the energy per atom computed with DFT, POD-I, and POD-II as a function of volume per atom for the anatase, rutile, and brookite crystal structures. Both POD-I and POD-II potentials smoothly reproduce the energy as function of the lattice volume of rutile, anatase, and brookite. It is crucial that the energies of similar structures are reproduced smoothly. If the energy errors on the order of 2 meV/atom were completely stochastic, the potential energy surface would be rugged and thus unsuitable for MD simulations. Table 4 summarizes the cohesive energies and unit cell volumes for the rutile, anatase, and brookite structures. The agreement between the values predicted by the POD potentials and their DFT references is excellent.

Crystal phase	DFT		POD-I		POD-II	
	$E_0$	$V_0$	$E_0$	$V_0$	$E_0$	$V_0$
Anatase	0.000	11.71	0.001	10.70	0.005	10.70
Rutile	0.033	10.68	0.037	10.85	0.034	10.68
Brookite	0.016	11.01	0.016	11.01	0.016	11.01

Table 4: Cohesive energies per atom  $E_0$  (eV/atom) and unit cell volumes per atom  $V_0$  (Å<sup>3</sup>/atom) for three different TiO<sub>2</sub> phases as computed using density-functional theory (DFT) and POD potentials with  $N_f = 30$ .

In this study, the phase energies of the TiO<sub>2</sub> compound were the primary focus, since smoothly reproducing the phase energies is essential for MD simulations. The quadratic POD potential provided more accurate predictions than the other potentials. The reference data set was restricted to periodic bulk structures. As a consequence, the constructed TiO<sub>2</sub> potentials can therefore not be expected to describe surface models (slab structures) or liquid phase accurately. Additional training data will be needed to further improve these potentials for other target applications.

## 6. Conclusions

We have developed proper orthogonal descriptors for multi-element chemical systems based on the orthogonal expansion of the radial and angular components of the parametrized potentials. In our work, the parametrized potentials are designed to provide a rich and diverse representation of two-body and three-body interactions. Owing to the exponential convergence of the orthogonal expansion, the number of basis functions needed to reach convergence in energy and force errors typically ranges from 30 to 60. We

compose the proper orthogonal descriptors in two different ways to construct two different interatomic potentials. The first POD potential expresses the energy of each atom as a linear combination of proper orthogonal descriptors, while the second POD potential expresses the energy as a linear and quadratic combination of the descriptors. Their computational complexity is similar and independent of the number of elements in the system.

As the performance of an interatomic potential critically depends on the hyperparameters, we have formulated a bilevel minimization problem to simultaneously optimize both the potential coefficients and hyperparameters. The objective function of the bilevel minimization problem is replaced with a surrogate model using polynomial interpolation. The gradient descent algorithm is used with randomly sampled initial guesses to minimize the surrogate loss function for the hyperparameters and the potential coefficients.

We have demonstrated the two POD potentials for indium phosphide and titanium dioxide, and compared their performance to that of multi-element SNAP and ACE potentials. For all potentials, increasing the number of basis functions usually improves prediction of energies and forces. The optimal number of basis functions appears to be in the range between 30 and 60. When the number of basis functions is more than 60, the accuracy gain is very modest while the computational cost is substantially increased. When the number of basis functions is less than 30, there is still much to be gained by increasing the number of basis functions to improve the prediction accuracy. These observations are consistent with the previous results [23] for single-element systems.

The quadratic POD potential was shown to provide much more accurate prediction of energies and forces than the linear POD potential at the same computational cost. The improvement stems from the composition of two-body and three-body descriptors to construct four-body descriptors without increasing the computational complexity of the resulting potential. The quadratic POD potential was also found to be more accurate than both ACE and SNAP potentials. In particular, the quadratic POD potential with 30 basis functions provided as accurate predictions as ACE and SNAP potentials with 91 basis functions for indium phosphite and titanium dioxide. A crucial advantage of POD potentials for multi-element chemical systems is that their computational complexity is independent of the number of elements, whereas the complexity of both ACE and SNAP potentials is dependent on the number of elements.

The ideas presented in this paper can be extended to both empirical

and machine learning potentials. The two-body orthogonal basis functions developed herein can be used as radial basis functions in power spectrum, bispectrum, SOAP and ACE descriptors. Moreover, instead of fitting the parameters of empirical potentials, one can use the proper orthogonal decomposition to construct an orthogonal basis for the parametric manifold of empirical potentials. We believe that this approach may improve not only the accuracy but also the transferability of existing empirical potentials.

The method of constructing higher-body descriptors from lower-body descriptors described in this paper is extensible to existing descriptors such as SOAP, SNAP, MTP, and ACE. For those descriptors, the resulting higher-body potential will retain the same computational complexity as the original potential. Likewise, it can be used to compose different empirical potentials to produce higher-body empirical potentials.

## Acknowledgements

I would like to thank all members of the CESMIX center at MIT for fruitful and invaluable discussions leading me to the ideas presented in this work. I want to thank Jaime Peraire, Robert M. Freund, Youssef Marzouk, Nicolas Hadjiconstantinou, Dionysios Sema, Yeongsu Cho, William Moses, Jayanth Mohan, Dallas Foster, Valentin Churavy, Mathew Swisher for the many discussions we have on a wide ranging of different topics related to this work. I would also like to thank Andrew Rohskopf, Axel Kohlmeyer and Aidan Thompson for fruitful discussions about LAMMPS implementation of POD potentials. I gratefully acknowledge the United States Department of Energy under contract DE-NA0003965 and the AFOSR Grant No. FA9550-22-1-0356 for supporting this work.

## References

- [1] M. S. Daw, M. I. Baskes, Embedded-atom method: Derivation and application to impurities, surfaces, and other defects in metals, *Physical Review B* 29 (12) (1984) 6443–6453. doi:10.1103/PhysRevB.29.6443.
- [2] F. H. Stillinger, T. A. Weber, Computer simulation of local order in condensed phases of silicon, *Physical Review B* 31 (8) (1985) 5262–5271. doi:10.1103/PhysRevB.31.5262.



- [3] J. Tersoff, New empirical approach for the structure and energy of covalent systems, *Physical Review B* 37 (12) (1988) 6991–7000. doi:10.1103/PhysRevB.37.6991.
- [4] M. Z. Bazant, E. Kaxiras, J. Justo, Environment-dependent interatomic potential for bulk silicon, *Physical Review B - Condensed Matter and Materials Physics* 56 (14) (1997) 8542–8552. arXiv:9704137, doi:10.1103/PhysRevB.56.8542.
- [5] D. W. Brenner, O. A. Shenderova, J. A. Harrison, S. J. Stuart, B. Ni, S. B. Sinnott, A second-generation reactive empirical bond order (REBO) potential energy expression for hydrocarbons, *Journal of Physics Condensed Matter* 14 (4) (2002) 783–802. doi:10.1088/0953-8984/14/4/312.
- [6] A. C. Van Duin, S. Dasgupta, F. Lorant, W. A. Goddard, ReaxFF: A reactive force field for hydrocarbons, *Journal of Physical Chemistry A* 105 (41) (2001) 9396–9409. doi:10.1021/jp004368u.
- [7] A. P. Bartók, R. Kondor, G. Csányi, On representing chemical environments, *Physical Review B - Condensed Matter and Materials Physics* 87 (18) (2013). arXiv:1209.3140, doi:10.1103/PhysRevB.87.184115.
- [8] J. Behler, Perspective: Machine learning potentials for atomistic simulations, *Journal of Chemical Physics* 145 (17) (2016). doi:10.1063/1.4966192.
- [9] G. Dusson, M. Bachmayr, G. Csányi, R. Drautz, S. Etter, C. van der Oord, C. Ortner, Atomic cluster expansion: Completeness, efficiency and stability, *Journal of Computational Physics* 454 (2022) 110946. arXiv:1911.03550, doi:10.1016/j.jcp.2022.110946.  
URL <https://www.sciencedirect.com/science/article/pii/S0021999122000080>
- [10] J. Behler, M. Parrinello, Generalized neural-network representation of high-dimensional potential-energy surfaces, *Physical Review Letters* 98 (14) (2007). doi:10.1103/PhysRevLett.98.146401.
- [11] J. Behler, Atom-centered symmetry functions for constructing high-dimensional neural network potentials, *Journal of Chemical Physics* 134 (7) (2011). doi:10.1063/1.3553717.

- [12] J. Behler, Representing potential energy surfaces by high-dimensional neural network potentials (2014). doi:10.1088/0953-8984/26/18/183001.
- [13] A. P. Bartók, M. C. Payne, R. Kondor, G. Csányi, Gaussian approximation potentials: The accuracy of quantum mechanics, without the electrons, *Physical Review Letters* 104 (13) (2010). arXiv:0910.1019, doi:10.1103/PhysRevLett.104.136403.
- [14] S. Fujikake, V. L. Deringer, T. H. Lee, M. Krynski, S. R. Elliott, G. Csányi, Gaussian approximation potential modeling of lithium intercalation in carbon nanostructures, *Journal of Chemical Physics* 148 (24) (2018). arXiv:1712.04472, doi:10.1063/1.5016317.
- [15] W. J. Szlachta, A. P. Bartók, G. Csányi, Accuracy and transferability of Gaussian approximation potential models for tungsten, *Physical Review B - Condensed Matter and Materials Physics* 90 (10) (2014). doi:10.1103/PhysRevB.90.104108.
- [16] A. P. Thompson, L. P. Swiler, C. R. Trott, S. M. Foiles, G. J. Tucker, Spectral neighbor analysis method for automated generation of quantum-accurate interatomic potentials, *Journal of Computational Physics* 285 (2015) 316–330. doi:10.1016/j.jcp.2014.12.018.
- [17] M. A. Wood, A. P. Thompson, Extending the accuracy of the SNAP interatomic potential form, *Journal of Chemical Physics* 148 (24) (2018). arXiv:1711.11131, doi:10.1063/1.5017641.
- [18] I. I. Novoselov, A. V. Yanilkin, A. V. Shapeev, E. V. Podryabinkin, Moment tensor potentials as a promising tool to study diffusion processes, *Computational Materials Science* 164 (2019) 46–56. arXiv:1812.02946, doi:10.1016/j.commatsci.2019.03.049.
- [19] A. V. Shapeev, Moment tensor potentials: A class of systematically improvable interatomic potentials, *Multiscale Modeling and Simulation* 14 (3) (2016) 1153–1173. arXiv:1512.06054, doi:10.1137/15M1054183.
- [20] R. Drautz, Atomic cluster expansion for accurate and transferable interatomic potentials, *Physical Review B* 99 (1) (2019). doi:10.1103/PhysRevB.99.014104.

- [21] R. Drautz, Atomic cluster expansion of scalar, vectorial, and tensorial properties including magnetism and charge transfer, *Physical Review B* 102 (2) (2020). [arXiv:2003.00221](#), [doi:10.1103/PhysRevB.102.024104](#).
- [22] Y. Zuo, C. Chen, X. Li, Z. Deng, Y. Chen, J. Behler, G. Csányi, A. V. Shapeev, A. P. Thompson, M. A. Wood, S. P. Ong, Performance and Cost Assessment of Machine Learning Interatomic Potentials, *Journal of Physical Chemistry A* 124 (4) (2020) 731–745. [arXiv:1906.08888](#), [doi:10.1021/acs.jpca.9b08723](#).
- [23] N. C. Nguyen, A. Rohskopf, Proper Orthogonal Descriptors for Efficient and Accurate Interatomic Potentials (aug 2022). [arXiv:2209.02362](#), [doi:10.48550/arxiv.2209.02362](#).  
URL <http://arxiv.org/abs/2209.02362>
- [24] M. Barrault, N. C. Nguyen, Y. Maday, A. T. Patera, An “Empirical Interpolation” Method: Application to Efficient Reduced-Basis Discretization of Partial Differential Equations, *Comptes Rendus Mathématique* 339 (9) (2004) 667–672. [doi:10.1016/j.crma.2004.08.006](#).  
URL <http://linkinghub.elsevier.com/retrieve/pii/S1631073X04004248>  
<http://www.sciencedirect.com/science/article/pii/S1631073X04004248>
- [25] S. Boyaval, C. L. Bris, Y. Maday, N. C. Nguyen, A. T. Patera, A reduced basis approach for variational problems with stochastic parameters: Application to heat conduction with variable Robin coefficient, *Computer Methods in Applied Mechanics and Engineering* 198 (41-44) (2009) 3187–3206. [doi:10.1016/j.cma.2009.05.019](#).  
URL <http://linkinghub.elsevier.com/retrieve/pii/S0045782509002114>
- [26] M. a. Grepl, Y. Maday, N. C. Nguyen, A. T. Patera, Efficient reduced-basis treatment of nonaffine and nonlinear partial differential equations, *ESAIM: Mathematical Modelling and Numerical Analysis* 41 (3) (2007) 575–605. [doi:10.1051/m2an:2007031](#).  
URL <http://www.esaim-m2an.org/10.1051/m2an:2007031>
- [27] G. Rozza, D. B. P. Huynh, A. T. Patera, Reduced basis approximation and a posteriori error estimation for affinely parametrized elliptic coe-

- cive partial differential equations: Application to transport and continuum mechanics, *Archives Computational Methods in Engineering* 15 (4) (2008) 229–275.
- [28] N. C. Nguyen, A multiscale reduced-basis method for parametrized elliptic partial differential equations with multiple scales, *Journal of Computational Physics* 227 (23) (2008) 9807–9822.  
URL <http://www.scopus.com/inward/record.url?eid=2-s2.0-53349103005&partnerID=40&md5=64852a2fac4b34c956379f980e2cf264>
- [29] L. Sirovich, Turbulence and the Dynamics of Coherent Structures, Part 1: Coherent Structures, *Quarterly of Applied Mathematics* 45 (3) (1987) 561–571.
- [30] M. A. Cusentino, M. A. Wood, A. P. Thompson, Explicit Multielement Extension of the Spectral Neighbor Analysis Potential for Chemically Complex Systems, *The Journal of Physical Chemistry A* 124 (26) (2020) 5456–5464. doi:10.1021/acs.jpca.0c02450.  
URL <https://doi.org/10.1021/acs.jpca.0c02450>
- [31] A. P. Thompson, H. M. Aktulga, R. Berger, D. S. Bolintineanu, W. M. Brown, P. S. Crozier, P. J. in ’t Veld, A. Kohlmeyer, S. G. Moore, T. D. Nguyen, R. Shan, M. J. Stevens, J. Tranchida, C. Trott, S. J. Plimpton, LAMMPS - a flexible simulation tool for particle-based materials modeling at the atomic, meso, and continuum scales, *Computer Physics Communications* 271 (2022) 108171. doi:10.1016/j.cpc.2021.108171.
- [32] D. N. Nichols, D. S. Rimai, R. J. Sladek, Elastic anharmonicity of InP: Its relationship to the high pressure transition, *Solid State Communications* 36 (8) (1980) 667–669. doi:10.1016/0038-1098(80)90205-7.
- [33] M. Matsui, M. Akaogi, Molecular dynamics simulation of the structural and physical properties of the four polymorphs of tio2, *Molecular Simulation* 6 (4-6) (1991) 239–244. doi:10.1080/08927029108022432.
- [34] P. M. Oliver, G. W. Watson, E. T. Kelsey, S. C. Parker, Atomistic simulation of the surface structure of the TiO2 polymorphs rutile and anatase, *Journal of Materials Chemistry* 7 (3) (1997) 563–568. doi:10.1039/a606353e.

- [35] V. Swamy, J. D. Gale, Transferable variable-charge interatomic potential for atomistic simulation of titanium oxides, *Physical Review B - Condensed Matter and Materials Physics* 62 (9) (2000) 5406–5412. doi:10.1103/PhysRevB.62.5406.
- [36] V. Swamy, J. D. Gale, L. S. Dubrovinsky, Atomistic simulation of the crystal structures and bulk moduli of TiO<sub>2</sub> polymorphs, *Journal of Physics and Chemistry of Solids* 62 (5) (2001) 887–895. doi:10.1016/S0022-3697(00)00246-8.
- [37] S. Y. Kim, N. Kumar, P. Persson, J. Sofo, A. C. Van Duin, J. D. Kubicki, Development of a ReaxFF reactive force field for titanium dioxide/water systems, *Langmuir* 29 (25) (2013) 7838–7846. doi:10.1021/la4006983.
- [38] Y. T. Cheng, T. R. Shan, T. Liang, R. K. Behera, S. R. Phillpot, S. B. Sinnott, A charge optimized many-body (comb) potential for titanium and titania, *Journal of Physics Condensed Matter* 26 (31) (2014). doi:10.1088/0953-8984/26/31/315007.
- [39] N. Artrith, A. Urban, An implementation of artificial neural-network potentials for atomistic materials simulations: Performance for TiO<sub>2</sub>, *Computational Materials Science* 114 (2016) 135–150. doi:10.1016/j.commatsci.2015.11.047.
- [40] C. Schran, F. L. Thiemann, P. Rowe, E. A. Müller, O. Marsalek, A. Michaelides, Machine learning potentials for complex aqueous systems made simple, *Proceedings of the National Academy of Sciences of the United States of America* 118 (38) (2021). arXiv:2106.00048, doi:10.1073/pnas.2110077118.
- [41] M. F. Andrade, H. Y. Ko, L. Zhang, R. Car, A. Selloni, Free energy of proton transfer at the water-TiO<sub>2</sub> interface from: ab initio deep potential molecular dynamics, *Chemical Science* 11 (9) (2020) 2335–2341. doi:10.1039/c9sc05116c.